ACS APPLIED MATERIALS & INTERFACES

www.acsami.org Research Article

Self-Powered 2D Material-Based pH Sensor and Photodetector Driven by Monolayer $MoSe_2$ Piezoelectric Nanogenerator

Peng Li* and Zekun Zhang

Cite This: *ACS Appl. Mater. Interfaces* 2020, 12, 58132–58139 Read Online

ACCESS | Metrics & More | Article Recommendations | Supporting Information

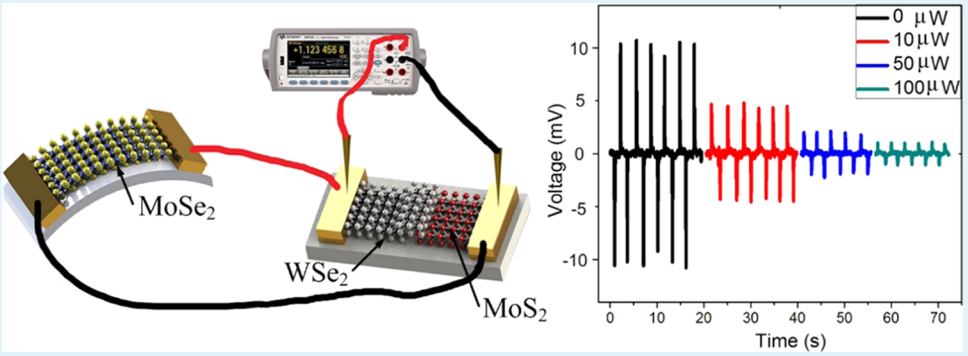

ABSTRACT: The large piezoelectricity of monolayer $MoSe_2$, which is predicted to be stronger than that of all of the other group VIB transition-metal dichalcogenides (including MoS_2), has only been theoretically investigated. Here, we report experimental evidence of in-plane piezoelectricity in $MoSe_2$. Monolayer single-crystalline $MoSe_2$ flake derived from chemical vapor deposition demonstrates a peak output voltage of 60 mV at 0.6% strain, which is ∼50% larger than that of MoS_2. Piezoelectric signal along the armchair orientation of $MoSe_2$ is ∼6 times larger than that along the zigzag orientation, indicative of strong anisotropic piezoelectricity. Piezoelectric nanogenerator based on a single $MoSe_2$ flake illustrates remarkable electromechanical conversion ability, and thus is able to noninvasively monitor vital health signs, such as respiratory rate and heart rate. Despite the extremely small size, $MoSe_2$ nanogenerator is able to drive pH sensor based on MoS_2 and photodetector based on MoS_2/WSe_2 heterojunction due to the outstanding piezoelectricity of $MoSe_2$ and the ultralow power consumption of two-dimensional (2D) material sensors. The self-powered, solely 2D-material-based sensor units demonstrate superb sensing performance. Therefore, the discovery of piezoelectricity in monolayer $MoSe_2$ provides a route for achieving self-powered atomic-scale electromechanical systems that could stimulate further fundamental research and potential applications.

KEYWORDS: *$MoSe_2$, piezoelectric, nanogenerator, self-powered sensing, pH sensor, photodetector*

1. INTRODUCTION

Two-dimensional (2D) materials have drawn significant attention in both fundamental and applied research due to their unique physical and chemical properties.[1−4] Their extremely large surface-to-volume ratio, exceptional electrical properties, ultralow noise level, and facile preparation make them promising candidates for sensing applications, such as ion, gas, and optical sensing.[5−16] Compared with traditional microelectromechanical systems (MEMS) sensors, 2D material sensors exhibit superior sensitivity, much smaller size and weight, lower energy consumption, and better flexibility.[17,18] However, the power supply has become the bottleneck of 2D material sensing technology. 2D material sensors reported so far exclusively rely on macroscopic external (battery) power supply, which hinders the miniaturization of the whole sensor unit. Additionally, with the rapid development of sensor networks and the Internet of things (IoT), trillions of sensor units will be needed and distributed on the earth. Replacing or charging trillions of batteries that have a limited lifetime will be impossible work. In view of the large amount of mechanical energy existing in the surrounding environment and human body, it is a promising way of utilizing piezoelectric nanogenerator[19,20] to harvest the energy and realize a self-powered 2D material sensor unit.

Piezoelectric materials allow reversible interconversion between mechanical energy and electrical energy.[21−23] Mechanical stress applied to these materials influences the electronic polarization, which results in internal electric fields

Received: October 7, 2020
Accepted: December 6, 2020
Published: December 16, 2020

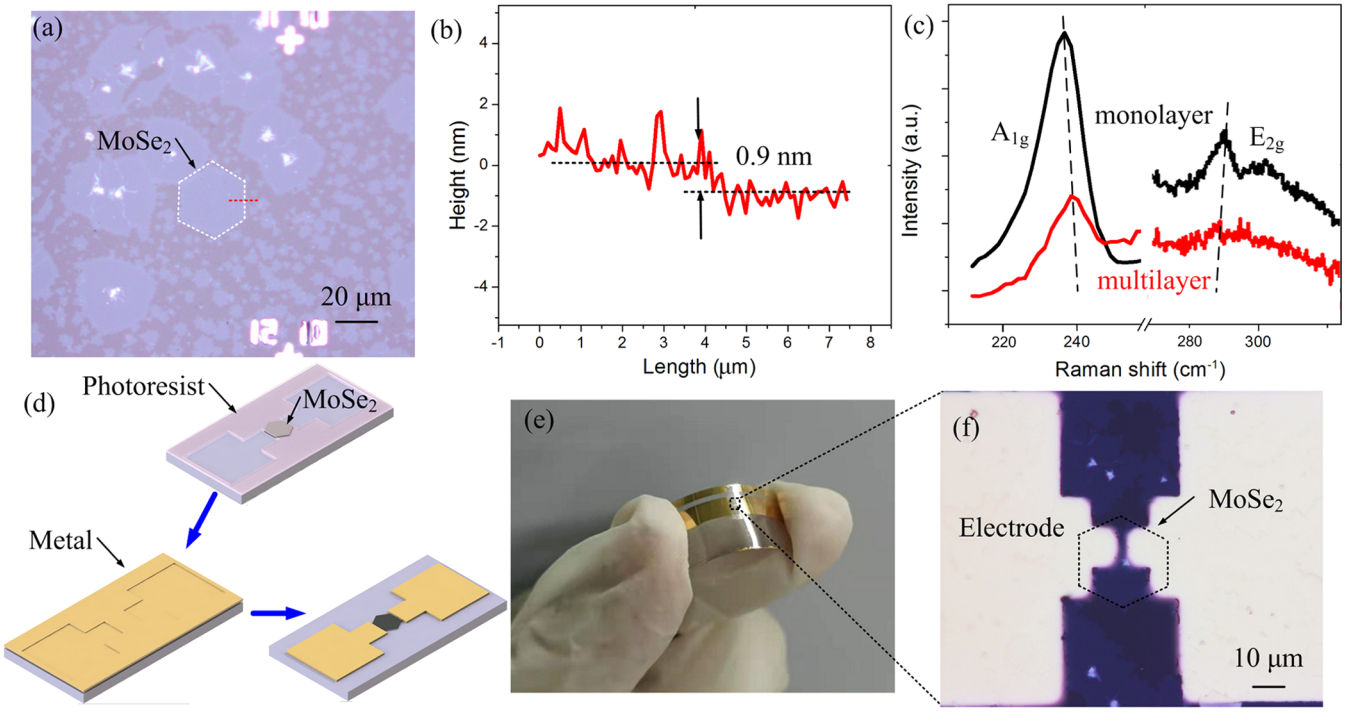

Figure 1. (a) Optical microscopy image of the $MoSe_2$ flakes on a PET substrate. (b) AFM height profile of a $MoSe_2$ flake extracted from a (red dash line), which demonstrates that the thickness is ~0.9 nm. (c) Raman spectra of the CVD monolayer $MoSe_2$ and mechanically exfoliated multilayer $MoSe_2$. (d) $MoSe_2$ piezoelectric device fabrication process. The metal electrodes are defined by photolithography, followed by metal sputtering and the lift-off process. (e) Photo of the $MoSe_2$ piezoelectric nanogenerator. (f) Optical microscopy image of the $MoSe_2$ piezoelectric nanogenerator.

and vice versa. Piezoelectric materials play an important role in a rich variety of sensors, actuators, MEMS, flexible electronics, and energy harvesting. The limitation of conventional three-dimensional (3D) piezoelectric materials, including quartz and AlN, arises due to the brittle nature.[24] Besides, the growing requirement for miniaturized devices calls for low-dimensional piezoelectric materials. However, one-dimensional (1D) piezoelectric materials, such as ZnO, have poor compatibility with semiconductor fabrication procedures.[25,26] Wang first reported the piezoelectric effect of a monolayer MoS_2.[2727] Since then, monolayer transition-metal dichalcogenide (M-TMD) crystals have emerged as the next-generation piezoelectric materials.[28−35] M-TMD crystals are able to withstand a large strain of up to 11%,[36] indicating that they are resistant to mechanical failure. Compared with 1D piezoelectric materials, M-TMD crystals are compatible with semiconductor fabrication procedures due to their planar structure, and the synthesis of large-area M-TMDs has been realized.[37−39] Density functional theory (DFT) simulation[40] demonstrates that both the clamped-ion and relaxed-ion piezoelectric coefficients of 2D materials exhibit a monotonic periodic trend. According to this trend, $MoSe_2$ is predicted to be the strongest in group VIB TMDs (MX_2, M = Mo, W, and X = S, Se). However, most studies have focused on MoS_2,[41] and the piezoelectricity of $MoSe_2$ has not been experimentally investigated to the best of our knowledge.

Here, we experimentally investigated the remarkable in-plane piezoelectric properties of a monolayer $MoSe_2$ for the first time. The piezoelectric output signal of the monolayer single-crystalline $MoSe_2$ was ~50% larger than that of MoS_2. Atomically thin nanogenerator based on $MoSe_2$ was developed, which matched the size of 2D material sensors. We used the nanogenerator to power a pH sensor based on MoS_2 and a photodetector based on MoS_2/WSe_2 heterojunction without the need for a battery power source. The self-powered sensor units composed entirely of 2D materials demonstrated superb sensing performance.

2. EXPERIMENTAL SECTION

A 2 in quartz tube furnace was used for the chemical vapor deposition (CVD) synthesis of monolayer single-crystalline $MoSe_2$ flakes.[42] The flakes were then transferred on to a flexible poly(ethylene terephthalate) (PET) substrate, which was pretreated with oxygen plasma dry etching and heated to 80 °C for 10 min during the transfer process to enhance the adhesion force between substrate and $MoSe_2$. Tapping mode atomic force microscopy (AFM) characterization was carried out to determine the thickness of $MoSe_2$. The $MoSe_2$ flakes were further characterized by a Witec Alpha300R Confocal Raman microscopy with an excitation laser wavelength of 532 nm. The power of the laser was below 0.5 mW to avoid sample damage. Sequentially, piezoelectric nanogenerator devices were fabricated. Due to the macroscopic continuity of $MoSe_2$, we defined metal electrodes by regular photolithography instead of electron-beam lithography to largely reduce fabrication cost, followed by metal sputtering and lift-off process. Cr (10 nm) and Au (100 nm) were chosen as the electrodes to minimize the Schottky barrier and contact resistance. The metal electrodes on the target $MoSe_2$ flake were parallel to armchair orientation, and the gap between electrodes was 5 μm. A Cu conductive tape or Ag paste was used to connect the electrical leads and Au electrodes. The output voltage/current of $MoSe_2$ nanogenerator was measured by a Keysight 34470A multimeter.

3. RESULTS AND DISCUSSION

Figure 1a shows the optical microscopy image of $MoSe_2$ flakes on the PET substrate. Hexagonal-shaped single-crystalline $MoSe_2$ domains with edges parallel to the zigzag orientation

https://dx.doi.org/10.1021/acsami.0c18028
ACS Appl. Mater. Interfaces 2020, 12, 58132−58139

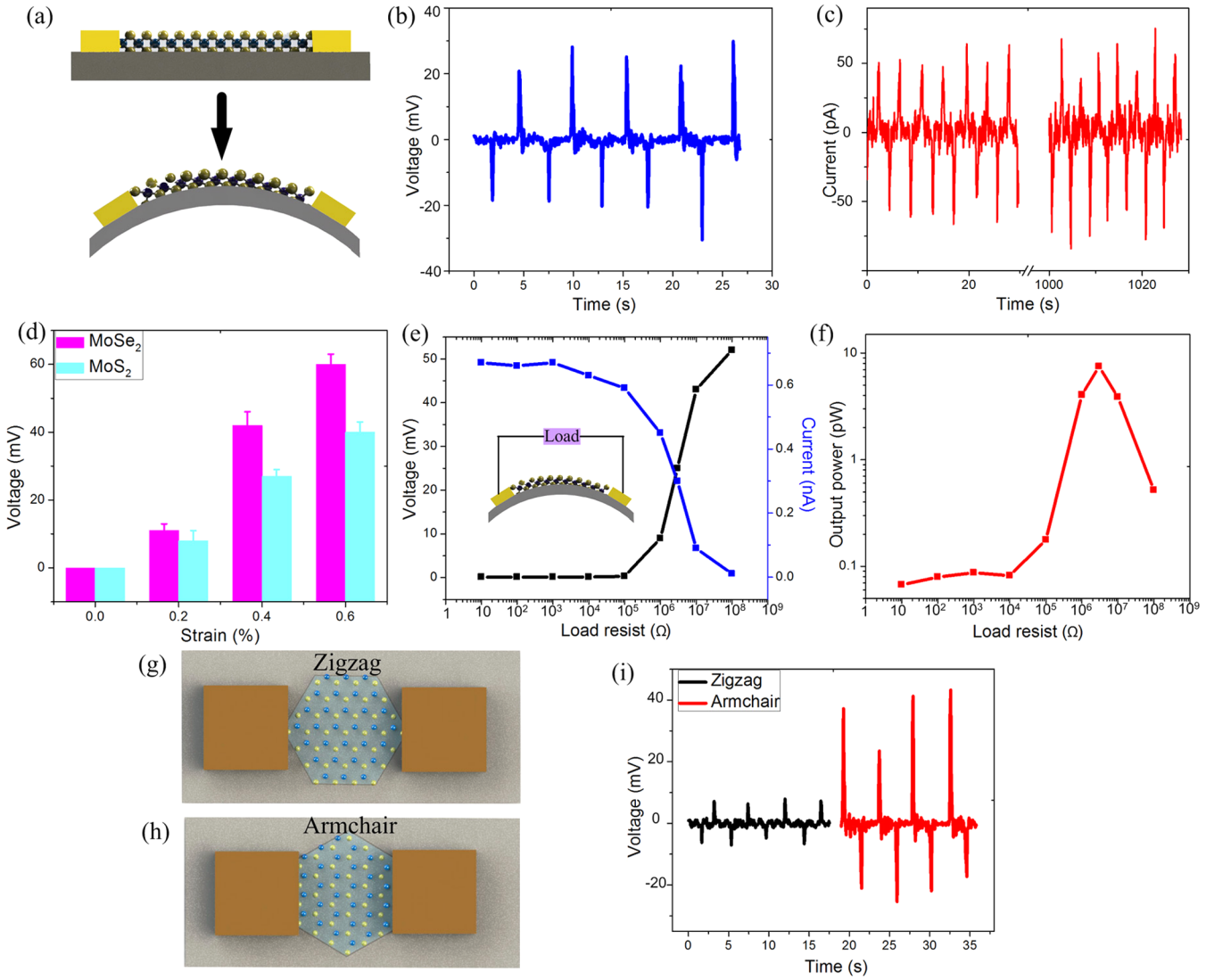

Figure 2. (a) Schematical diagram of the bending of the $MoSe_2$ piezoelectric nanogenerator. (b) Piezoelectric output voltage of the $MoSe_2$ piezoelectric nanogenerator under periodic bending and releasing. (c) Piezoelectric output current of the $MoSe_2$ piezoelectric nanogenerator. (d) Output voltages of the $MoSe_2$ and MoS_2 nanogenerators as a function of strain applied. (e) Dependence of the piezoelectric output voltage/current on load resistance. (f) Dependence of output power on load resistance. (g) Schematic view of the $MoSe_2$ piezoelectric nanogenerator with electrodes along the zigzag orientation. (h) Schematic view of the $MoSe_2$ piezoelectric nanogenerator with electrodes along the armchair orientation. (i) Piezoelectric signals of the $MoSe_2$ nanogenerator along the zigzag and armchair orientations, respectively.

were observed. Figure 1b is the AFM height profile of a typical flake extracted from Figure 1a (red dash line), which demonstrates that the thickness is ~0.9 nm, indicating a monolayer structure.[42] Figure 1c exhibits the Raman spectra of a CVD monolayer $MoSe_2$ sample and mechanically exfoliated multilayer $MoSe_2$ sample. Two characteristic peaks are Raman shifts attributed to the A_{1g} (~239 cm^{-1}) and E_{2g} (~286 cm^{-1}) phonon modes of $MoSe_2$, respectively.[42] The A_{1g} peak corresponds to the out-of-plane vibration of the atoms, whereas the E_{2g} peak corresponds to the in-plane vibration of the atoms. The A_{1g} and E_{2g} peaks are red-shifted and blue-shifted, respectively, from multilayer to monolayer, which is consistent with previous reports.[42] The sharp Raman peaks imply that the $MoSe_2$ samples studied in this work were high-quality crystals. Figure 1d demonstrates the fabrication procedure of the $MoSe_2$ piezoelectric nanogenerator. Figure 1e,f is the photo and optical microscopy image of a typical $MoSe_2$ piezoelectric nanogenerator device, respectively.

We systematically investigated the piezoelectric properties of a monolayer $MoSe_2$ for the first time. Unlike its bulk parent crystal, a monolayer $MoSe_2$ with a non-centrosymmetry structure is able to demonstrate an in-plane piezoelectric effect. As the PET substrate was bent, the monolayer $MoSe_2$ flake attached on its surface underwent uniaxial tensile/compressive strain (Figure 2a). Piezoelectric polarization charges were consequentially generated at two edges of the $MoSe_2$ flake and resulted in an output voltage/current peak. When the substrate was released, a reverse charge flow led to a voltage/current peak with an opposite sign. An out-of-plane piezoelectricity in M-TMDs could be generated from a strain gradient (flexoelectricity).[28,29] However, in our experiment, the strain applied was along the in-plane direction, and the electric signal detected was along the in-plane direction (the electrodes were parallel to the in-plane direction). As such, the piezoelectric output properties were mainly due to the in-plane piezoelectricity. Periodic bending and releasing PET

https://dx.doi.org/10.1021/acsami.0c18028
ACS Appl. Mater. Interfaces 2020, 12, 58132−58139

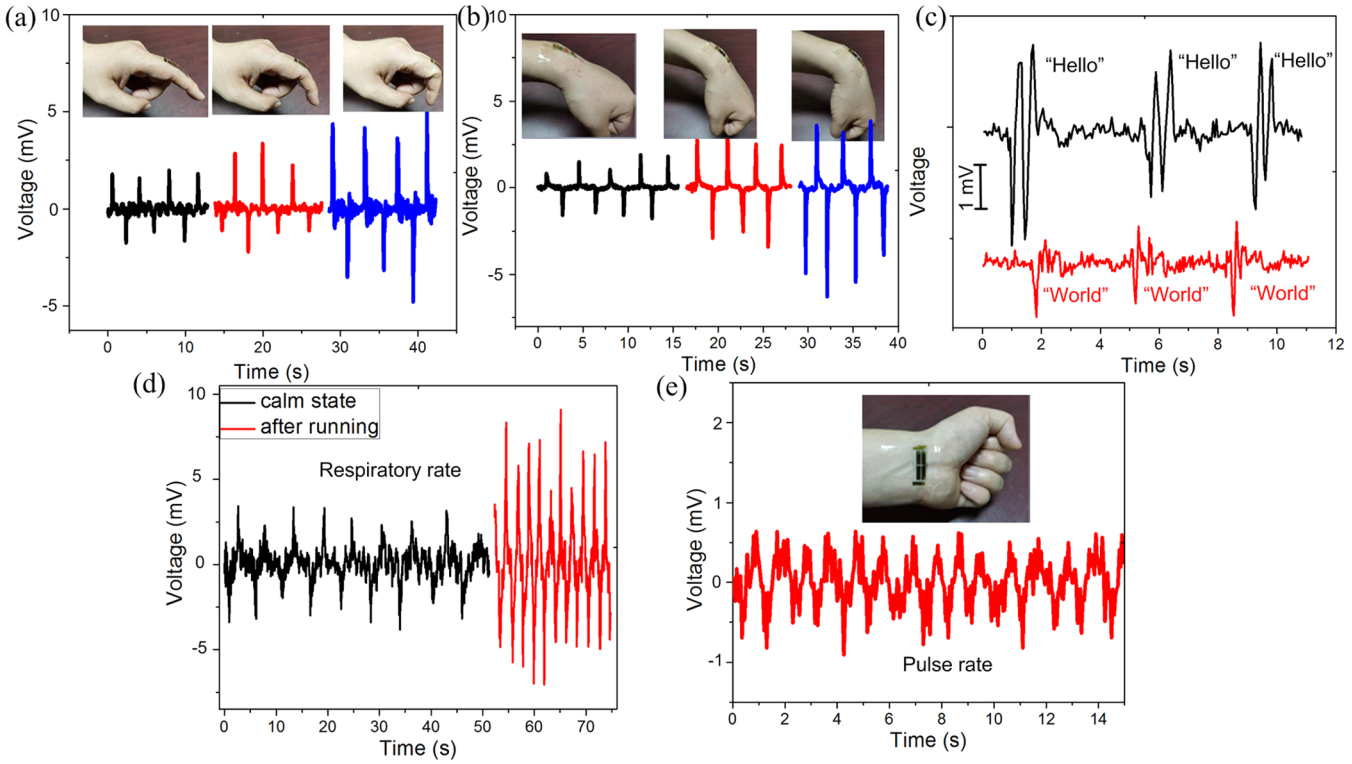

Figure 3. (a) Energy harvesting of the $MoSe_2$ nanogenerator from finger joint. (b) Energy harvesting of the $MoSe_2$ nanogenerator from the wrist. (c) Muscle movement during speech detected by attaching the $MoSe_2$ nanogenerator to the neck. (d) Respiratory rate detection by attaching the $MoSe_2$ nanogenerator on the chest. The frequency and amplitude of the piezoelectric signals have a significant difference when the tester is in calm state and after running. (e) Pulse rate detection by attaching the $MoSe_2$ nanogenerator on the wrist.

substrate led to periodic output voltage signals (Figure 2b) and current signals (Figure 2c). The cycle test demonstrated that the output signal of the $MoSe_2$ device was stable over a long period of operation time (Figure 2c) inasmuch as $MoSe_2$ has superb mechanical properties and is resistant to mechanical failure. The robust piezoelectricity makes $MoSe_2$ an ideal material choice for atomic-thin piezoelectric devices. No significant electrical output signal was observed from bare PET substrates without the $MoSe_2$ flake (Figure S1, Supporting Information), which further proves the piezoelectricity of $MoSe_2$. The magnitude of the output voltage is related to the uniaxial bending strain ε applied, which can be derived from the following equation[43]

$$\varepsilon = h/2r \tag{1}$$

where h is the thickness of the PET substrate (150 μm) and r is the PET substrate bending radius. The bending strain ε was limited to 0.6% to avoid slippage between the $MoSe_2$ flake and the PET substrate. As illustrated in Figure 2d, the output voltage of a typical $MoSe_2$ device was proportional to the bending strain ε. A monolayer single-crystalline $MoSe_2$ demonstrated a peak output voltage of 60 mV at a 0.6% strain, which was ~50% larger than that of the monolayer MoS_2 device fabricated and tested under the same condition (Figure 1d), indicative of the outstanding piezoelectric properties of $MoSe_2$. The reverse connection of $MoSe_2$ piezoelectric nanogenerators with the measuring equipment results in reverse output voltages (Figure S2, Supporting Information). Figure 2e,f illustrates the output characteristics of a typical $MoSe_2$ nanogenerator at 0.6% strain coupled to a load resistor. The output current reduced with an increasing load resistance value, whereas the voltage distributed on the load resistance changed in the opposite trend. The maximum output power of the $MoSe_2$ nanogenerator reached 7.5 pW at a load resistance of ~5 MΩ (Figure 2f). According to our experimental results, the piezoelectric coefficient e_{11} of $MoSe_2$ derived is ~435 pC/m, which is close to the simulation result reported (392 pC/m).[40] The equivalent capacitance of $MoSe_2$ and the system is[44]

$$C \approx t/R \tag{2}$$

where t is the full width at half-maximum of the voltage peak and R is the load resistance. The output electrical energy in one piezoelectric discharge event is[44]

$$W_E = V^2C/2 \tag{3}$$

where V is the peak output voltage. The mechanical energy stored in the monolayer $MoSe_2$ is

$$W_M = LWE\varepsilon^2/2 \tag{4}$$

where L and W are the length and width of $MoSe_2$, respectively, and E is Young's modulus of $MoSe_2$. The efficiency of converting mechanical energy to electrical energy is

$$\eta = W_E/W_M \tag{5}$$

According to our experimental results, $\eta \approx 7.2\%$. The dependence of the piezoelectric response on crystal orientation was investigated. The orientations were determined by the crystal shape because the edges of the hexagonal-shaped monolayer single-crystalline $MoSe_2$ are parallel to the zigzag direction. Devices with electrodes along the armchair and zigzag orientations were fabricated and tested under the same

https://dx.doi.org/10.1021/acsami.0c18028
ACS Appl. Mater. Interfaces 2020, 12, 58132−58139

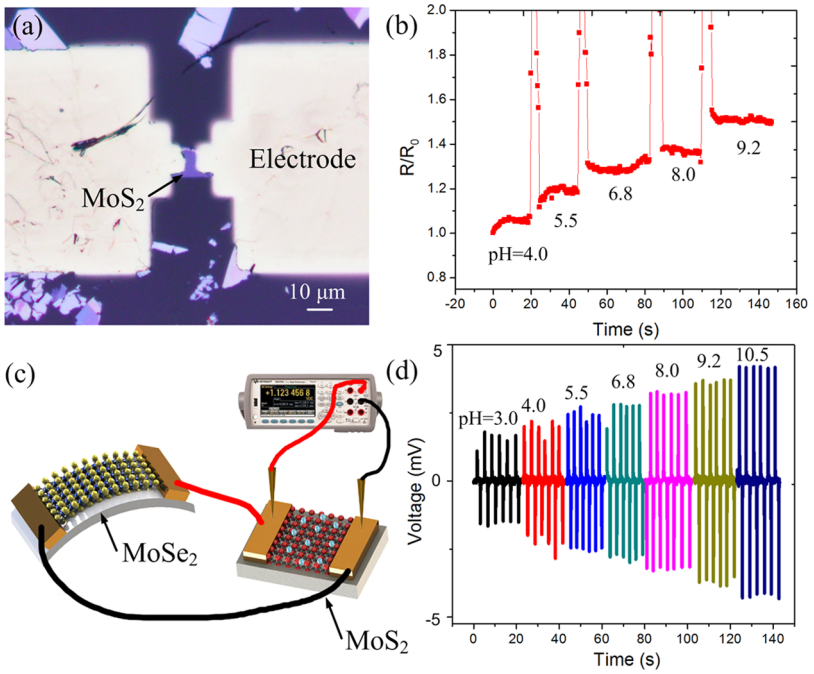

Figure 4. (a) Optical microscopy image of the MoS_2 pH sensor. (b) Dynamic resistance variation of the MoS_2 pH sensor. (c) Schematic view of the MoS_2 pH sensor driven by a $MoSe_2$ nanogenerator. (d) Sensing performance of the MoS_2 pH sensor driven by a $MoSe_2$ nanogenerator.

conditions (Figure 2g,h). Figure 2i clearly illustrates that the piezoelectric signals of the $MoSe_2$ nanogenerator at 0.4% strain along the armchair direction were ~6 times larger than that along the zigzag direction, indicating strong anisotropic piezoelectric properties. Therefore, the armchair is the optimum orientation for $MoSe_2$ piezoelectric devices.

Next, we explored the energy harvesting performance of the $MoSe_2$ nanogenerator from the human body. Figure 3a displays energy harvesting from finger bending by attaching the device to the tester's index finger joint. The piezoelectric output voltage is clearly enhanced as the bending degree increased from 30 to 90°. The device was then attached to the tester's wrist, and piezoelectric signals were also observed with magnitudes proportional to the wrist bending angles (Figure 3b). Therefore, the $MoSe_2$ piezoelectric device holds great potential in human activity monitoring. The $MoSe_2$ nanogenerator was attached to the neck of the tester to noninvasively monitor muscle movement during speech (Figure 3c). The obtained $V-t$ curves were clearly different when the tester pronounced different words, such as "hello" and "world". The waveforms illustrated similar characteristic peaks when the tester spoke the same word, indicative of good repeatability. It brings promise for the remote control of human/machine interfaces. Next, we demonstrated prototype wearable $MoSe_2$ devices that are capable of noninvasively monitoring vital health signs, such as respiratory rate and heart rate. The $MoSe_2$ nanogenerator was applied to monitor the respiratory rate by attaching it to the chest of the tester. Figure 3d depicts the obtained $V-t$ curves when the tester was in a calm state and right after running, respectively. Both the frequency and amplitude of the piezoelectric signal related to respiration significantly increased due to high-intensity exercise. $MoSe_2$ nanogenerator can monitor pulse rate by attaching it to the tester's wrist (Figure 3e). The magnitude of the piezoelectric signal was ~0.7 mV, and the pulse rate extracted was ~60/min. Therefore, the $MoSe_2$ piezoelectric device holds great potential in health-tracking wearable devices.[45−48]

After demonstrating the $MoSe_2$ nanogenerator's remarkable electromechanical conversion ability, we used the nanogenerator to drive a pH sensor based on MoS_2. Figure 4a is the optical microscopy image of a MoS_2 sensor. AFM characterization demonstrated that the thickness of the mechanically exfoliated multilayer MoS_2 flake was ~15 nm. Solutions with different pH values were sequentially introduced onto the MoS_2 sensor at room temperature. The resistance of the MoS_2 sensor measured by a Keysight 34470A multimeter rapidly increased as the pH value changed from 4.0 to 9.2 (Figure 4b). This process was repeated several times and demonstrated good repeatability (Figure S3, Supporting Information). The response rate of our MoS_2 pH sensor extracted was less than 10 s, which is mainly attributed to the superb electrical properties and large surface−volume ratio of MoS_2. The pH sensing mechanism of the MoS_2 sensor was investigated. The $I-V$ characteristic curve of a typical MoS_2 device demonstrates good linearity (Figure S4, Supporting Information), indicative of an insignificant Schottky barrier between MoS_2 and Cr/Au metal electrodes.[41,42] Therefore, the output signals are mainly attributed to the MoS_2 flake instead of metal contact during sensing. The resistivity of MoS_2 can be expressed by the equation

$$\rho = 1/nq\mu \tag{6}$$

where ρ is the resistivity, n is the electron density, q is the charge per carrier, and μ is the carrier mobility. MoS_2 is a n-type semiconductor, so negatively charged electrons are majority carriers. The OH^- ion adsorption serves as a negative gate voltage, which reduces the electron density n in MoS_2 and results in larger resistivity. In contrast, the H^+ ion adsorption increases the electron density and reduces the resistivity. We used the $MoSe_2$ nanogenerator to power the MoS_2 pH sensor by connecting them in series to form a loop (Figure 4c). A

https://dx.doi.org/10.1021/acsami.0c18028
ACS Appl. Mater. Interfaces 2020, 12, 58132−58139

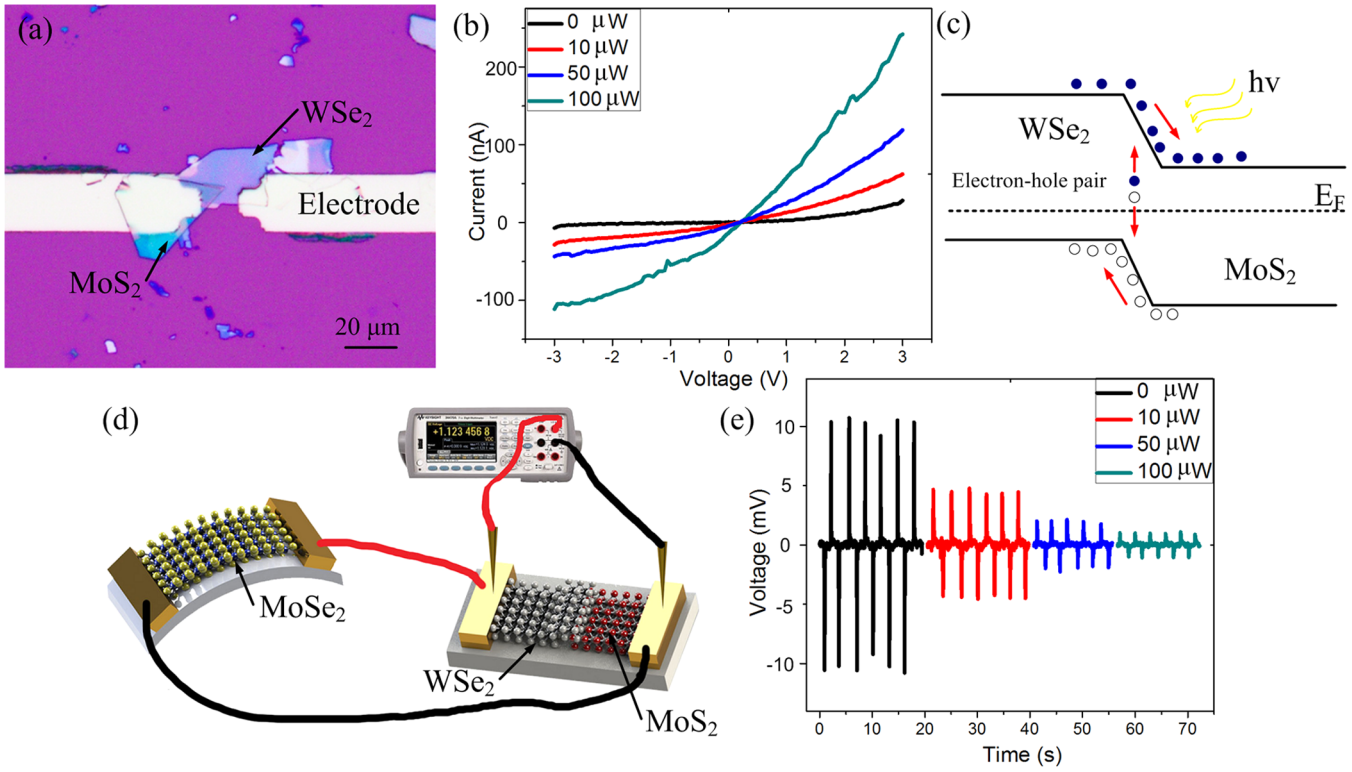

Figure 5. (a) Optical microscopy image of the MoS_2/WSe_2 heterojunction photodetector. (b) *I*−*V* curves of the MoS_2/WSe_2 heterojunction under different intensities of illumination. (c) Energy band structure of the MoS_2/WSe_2 heterojunction under illumination. (d) Schematic view of the MoS_2/WSe_2 heterojunction photodetector driven by $MoSe_2$ nanogenerator. (e) Sensing performance of the MoS_2/WSe_2 heterojunction photodetector driven by a $MoSe_2$ nanogenerator.

clear sensitivity to pH change was observed (Figure 4d). As the pH value changed from 3.0 to 10.5, the resistance of the MoS_2 sensor increased and the voltage across the MoS_2 sensor varied from 1.6 to 4.2 mV accordingly. As such, the self-powered MoS_2 pH sensor driven by the $MoSe_2$ nanogenerator demonstrated good sensing performance without a need for a battery power source. Due to the extremely small size of the $MoSe_2$ nanogenerator and MoS_2 sensor, we successfully integrated them on a 1 cm × 1 cm PET substrate. The integrated self-powered sensing unit illustrated the same pH sensing performance as depicted in Figure 4d.

The 2D material heterojunction is another fundamental device building block for sensing the applications. The MoS_2/WSe_2 photodetector was chosen as a typical 2D material heterojunction sensor. Figure 5a is the optical microscopy image of a MoS_2/WSe_2 atomically thin vertical heterojunction. Multilayer MoS_2 and WSe_2 flakes were both derived from mechanical exfoliation. We used a white light source to illuminate the photodetector, and the estimated optical power distributed on the heterojunction was 10, 50, and 100 μW, respectively. The *I*−*V* characteristic curves derived by an Agilent B1500A semiconductor parameter analyzer demonstrated that the current of the MoS_2/WSe_2 heterojunction drastically increased under illumination (Figure 5b). The photoresponsivity acquired was 1.9 mA/W. As the light was turned off, the current of the MoS_2/WSe_2 heterojunction rapidly changed back to the original value. This process was repeated several times and demonstrated good repeatability. The illumination results in photon absorption and the excitation of electron−hole pairs in the heterojunction region, which can be extracted by applying a bias (Figure 5c). As such, the MoS_2/WSe_2 heterostructure converts the energy of photon absorbed into photocurrent, and its resistivity reduces accordingly. Compared with a photodetector based on a single 2D material, this heterojunction structure largely increases sensitivity by separating the photogenerated electron−hole pairs, which results in enhanced carrier lifetime and photoresponsivity. We used the $MoSe_2$ nanogenerator to power the MoS_2/WSe_2 photodetector (Figure 5d). The voltage across the MoS_2/WSe_2 heterojunction drastically decreased from 10 to 1.2 mV as the illumination intensity varied from 0 to 100 μW, inasmuch as the resistance of heterojunction reduced significantly (Figure 5e). Therefore, the self-powered 2 material heterojunction photodetector driven by a $MoSe_2$ nanogenerator demonstrated superb sensing performance without the need of a battery power source.

4. CONCLUSIONS

We systematically investigated the remarkable in-plane piezoelectric properties of a monolayer $MoSe_2$ for the first time. Monolayer single-crystalline $MoSe_2$ demonstrated a peak output voltage of 60 mV at 0.6% strain, which was ∼50% larger than that of MoS_2. $MoSe_2$ illustrated a strong anisotropic piezoelectric response. The piezoelectric signal along the armchair direction was ∼6 times larger than that along the zigzag direction. We used a $MoSe_2$ nanogenerator to drive a MoS_2 pH sensor and a MoS_2/WSe_2 photodetector, respectively, by harvesting ambient mechanical energy without a need for a battery power source. Our research offers a platform for the fundamental investigation of electronic polarization and electromechanical conversion in 2D piezoelectric materials and

https://dx.doi.org/10.1021/acsami.0c18028
ACS Appl. Mater. Interfaces 2020, 12, 58132−58139

provides a route for achieving novel self-powered atomic-scale electromechanical systems.

■ ASSOCIATED CONTENT

Supporting Information

The Supporting Information is available free of charge at https://pubs.acs.org/doi/10.1021/acsami.0c18028.

Output properties of bare PET substrate without $MoSe_2$, switching polarity test of $MoSe_2$ piezoelectric nanogenerators, repeatability of the MoS_2 pH sensor, *I*−*V* characteristic of the MoS_2 sensor, CVD synthesis of $MoSe_2$, MoS_2 pH sensor, and MoS_2/WSe_2 photodetector fabrication procedure (PDF)

■ AUTHOR INFORMATION

Corresponding Author

Peng Li − *State Key Laboratory of Precision Measurement Technology and Instruments, Department of Precision Instruments, Tsinghua University, Beijing 100084, China;* orcid.org/0000-0002-8791-7465; Email: pengli@mail.tsinghua.edu.cn

Author

Zekun Zhang − *State Key Laboratory of Precision Measurement Technology and Instruments, Department of Precision Instruments, Tsinghua University, Beijing 100084, China*

Complete contact information is available at: https://pubs.acs.org/10.1021/acsami.0c18028

Notes

The authors declare no competing financial interest.

■ ACKNOWLEDGMENTS

This work was supported by the National Natural Science Foundation of China (51775306) and the Beijing Municipal Natural Science Foundation (4192027).

■ REFERENCES

(1) Taniguchi, T.; Nurdiwijayanto, L.; Li, S.; Lim, H. E.; Miyata, Y.; Lu, X.; Ma, R.; Tang, D. M.; Ueda, S.; Tsukagoshi, K.; Sasaki, T.; Osada, M. On/Off Boundary of Photocatalytic Activity Between Single- and Bilayer MoS_2. *ACS Nano* **2020**, *14*, 6663−6672.

(2) Lee, C.; Wei, X. D.; Kysar, J. W.; Hone, J. Measurement of the Elastic Properties and Intrinsic Strength of Monolayer Graphene. *Science* **2008**, *321*, 385−388.

(3) Huang, Z.; Han, W.; Tang, H.; Ren, L.; Chander, D. S.; Qi, X.; Zhang, H. Photoelectrochemical-Type Sunlight Photodetector Based on MoS_2/Graphene Heterostructure. *2D Mater.* **2015**, *2*, No. 035011.

(4) Cha, E.; Patel, M. D.; Park, J.; Hwang, J.; Prasad, V.; Cho, K.; Choi, W. 2D MoS_2 as an Efficient Protective Layer for Lithium Metal Anodes in High-Performance Li-S Batteries. *Nat. Nanotechnol.* **2018**, *13*, 337−344.

(5) Ohno, Y.; Maehashi, K.; Yamashiro, Y.; Matsumoto, K. Electrolyte-Gated Graphene Field-Effect Transistor for Detecting pH Protein Adsorption. *Nano Lett.* **2009**, *9*, 3318−3322.

(6) Ang, P. K.; Chen, W.; Wee, A. T. S.; Loh, K. P. Solution-Gated Epitaxial Graphene as pH Sensor. *J. Am. Chem. Soc.* **2008**, *130*, 14392−14393.

(7) Kuila, T.; Bose, S.; Khanra, P.; Mishra, A. K.; Kim, N. H.; Lee, J. H. Recent Advances in Graphene-Based Biosensors. *Biosens. Bioelectron.* **2011**, *26*, 4637−4648.

(8) Maity, A.; Sui, X.; Pu, H.; Bottum, K. J.; Jin, B.; Chang, J.; Zhou, G.; Lu, G.; Chen, J. Sensitive Field-Effect Transistor Sensors with Atomically Thin Black Phosphorus Nanosheets. *Nanoscale* **2020**, *12*, 1500−1512.

(9) Li, P.; Zhang, D.; Liu, J.; Chang, H.; Sun, Y.; Yin, N. Air-Stable Black Phosphorus Devices for Ion Sensing. *ACS Appl. Mater. Interfaces* **2015**, *7*, 24396−24402.

(10) Lee, K.; Gatensby, R.; McEvoy, N.; Hallam, T.; Duesberg, G. S. High-Performance Sensors Based on Molybdenum Disulfide Thin Films. *Adv. Mater.* **2013**, *25*, 6699−6702.

(11) Liu, Z.; Huang, J.; Wang, Q.; Zhou, J.; Ye, J.; Li, X.; Geng, Y.; Liang, Z.; Du, Y.; Tian, X. Indium Oxide-Black Phosphorus Composites for Ultrasensitive Nitrogen Dioxide Sensing at Room Temperature. *Sens. Actuators, B* **2020**, *308*, No. 127650.

(12) Zhang, D.; Yang, Z.; Li, P.; Pang, M.; Xue, Q. Flexible Self-powered High-Performance Ammonia Sensor Based on Au-Decorated $MoSe_2$ Nanoflowers Driven by Single Layer MoS_2-Flake Piezoelectric Nanogenerator. *Nano Energy* **2019**, *65*, No. 103974.

(13) Zhao, J.; Li, N.; Yu, H.; Wei, Z.; Liao, M.; Chen, P.; Wang, S.; Shi, D.; Sun, Q.; Zang, G. Highly Sensitive MoS_2 Humidity Sensor Array for Noncontact Sensation. *Adv. Mater.* **2017**, *29*, No. 1702076.

(14) Late, D. J.; Huang, Y. K.; Liu, B.; Acharya, J.; Shirodkar, S. N.; Luo, J. J.; Yan, A. M.; Charles, D.; Waghmare, U. V.; Dravid, V. P.; Rao, C. N. R. Sensing Behavior of Atomically Thin-Layered MoS_2 Transistors. *ACS Nano* **2013**, *7*, 4879−4891.

(15) Singh, E.; Singh, P.; Kim, K. S.; Yeom, G. Y.; Nalwa, H. S. Flexible Molybdenum Disulfide (MoS_2) Atomic Layers for Wearable Electronics and Optoelectronics. *ACS Appl. Mater. Interfaces* **2019**, *11*, 11061−11105.

(16) Nalwa, H. S. A Review of Molybdenum Disulfide (MoS_2) Based Photodetectors: from Ultra-Broadband, Self-Powered to Flexible Devices. *RSC Adv.* **2020**, *10*, 30529−30602.

(17) Kim, J. H.; Mirzaei, A.; Kim, H. W.; Kim, S. S. Flexible and Low Power CO Gas Sensor with Au-Functionalized 2D WS_2 Nanoflakes. *Sens. Actuators, B* **2020**, *313*, No. 128040.

(18) He, Q.; Zeng, Z.; Yin, Z.; Li, H.; Wu, X.; Huang, X.; Zhang, H. Fabrication of Flexible MoS_2 Thin-Film Transistor Arrays for Practical Gas-Sensing Applications. *Small* **2012**, *8*, 2994−2999.

(19) Park, K. I.; Xu, S.; Liu, Y.; Hwang, G. T.; Kang, S. J. L.; Wang, Z. L.; Lee, K. J. Piezoelectric $BaTiO_3$ Thin Film Nanogenerator on Plastic Substrates. *Nano Lett.* **2010**, *10*, 4939−4943.

(20) Huang, T.; Wang, C.; Yu, H.; Wang, H. Z.; Zhang, Q. H.; Zhu, M. F. Human Walking-Driven Wearable All-Fiber Triboelectric Nanogenerator Containing Electrospun Polyvinylidene Fluoride Piezoelectric Nanofibers. *Nano Energy* **2015**, *14*, 226−235.

(21) Dong, K.; Peng, X.; Wang, Z. L. Fiber/Fabric-Based Piezoelectric and Triboelectric Nanogenerators for Flexible/Stretchable and Wearable Electronics and Artificial Intelligence. *Adv. Mater.* **2020**, *32*, No. 1902549.

(22) Zhang, S.; Liu, Z. F.; Ruan, M. N.; Guo, Z. G.; Lei, E.; Zhao, W.; Zhao, D.; Wu, X.; Chen, D. Enhanced Piezoelectric-Effect-Assisted Photoelectrochemical Performance in ZnO Modified with Dual Cocatalysts. *Appl. Catal., B* **2020**, *262*, No. 118279.

(23) Jung, Y. H.; Hong, S. K.; Wang, H. S.; Han, J. H.; Pham, T. X.; Park, H.; Kim, J.; Kang, S.; Yoo, C. D.; Lee, K. J. Flexible Piezoelectric Acoustic Sensors and Machine Learning for Speech Processing. *Adv. Mater.* **2020**, *32*, No. 1904020.

(24) Gablech, I.; Klempa, J.; Pekarek, J.; Vyroubal, P.; Hrabina, J.; Hola, M.; Kunz, J.; Brodsky, J.; Neuzil, P. Simple and Efficient AlN-Based Piezoelectric Energy Harvesters. *Micromachines* **2020**, *11*, No. 143.

(25) Jin, C.; Hao, N. J.; Xu, Z.; Trase, I.; Nie, Y.; Dong, L.; Closson, A.; Chen, Z.; Zhang, J. X. J. Flexible Piezoelectric Nanogenerators Using Metal-Doped ZnO-PVDF Films. *Sens. Actuators, A* **2020**, *305*, No. UNSP 111912.

(26) Le, A. T.; Ahmadipour, M.; Pung, S. Y. A Review on ZnO-Based Piezoelectric Nanogenerators: Synthesis, Characterization Techniques, Performance Enhancement and Applications. *J. Alloys Compd.* **2020**, *844*, No. 156172.

(27) Wu, W.; Wang, L.; Li, Y.; Zhang, F.; Lin, L.; Niu, S.; Chenet, D.; Zhang, X.; Hao, Y.; Heinz, T. F.; Hone, J.; Wang, Z. L.

Piezoelectricity of Single-Atomic-layer MoS_2 for Energy Conversion and Piezotronics. *Nature* **2014**, *514*, 470−474.
(28) Kang, S.; Jeon, S.; Kim, S.; Seol, D.; Yang, H.; Lee, J.; Kim, Y. Tunable Out-of-Plane Piezoelectricity in Thin-Layered $MoTe_2$ by Surface Corrugation-Mediated Flexoelectricity. *ACS Appl. Mater. Interfaces* **2018**, *10*, 27424−27431.
(29) Seo, J.; Kim, Y.; Park, W. Y.; Son, J. Y.; Jeong, C. K.; Kim, H.; Kim, W. H. Out-of-Plane Piezoresponse of Monolayer MoS2 on Plastic Substrates Enabled by Highly Uniform and Layer-Controllable CVD. *Appl. Surf. Sci.* **2019**, *487*, 1356−1361.
(30) Lee, J. H.; Park, J. Y.; Cho, E. B.; Kim, T. Y.; Han, S. A.; Kim, T. H.; Liu, Y.; Kim, S. K.; Roh, C. J.; Yoon, H. J.; Ryu, H.; Seung, W.; Lee, J. S.; Lee, J.; Kim, S. W. Reliable Piezoelectricity in Bilayer WSe_2 for Piezoelectric Nanogenerators. *Adv. Mater.* **2017**, *29*, No. 1606667.
(31) Kim, J.; Lee, E.; Bhoyate, S.; An, T. K. Stable and High-Performance Piezoelectric Sensor via CVD Grown WS_2. *Nanotechnology* **2020**, *31*, No. 445203.
(32) Yu, S.; Rice, Q.; Tabibi, B.; Li, Q.; Seo, F. J. Piezoelectricity in WSe_2/MoS_2 Heterostructure Atomic Layers. *Nanoscale* **2018**, *10*, 12472−12479.
(33) Lee, G. J.; Lee, M. J.; Park, J. J.; Hyeon, D. Y.; Jeong, C. K.; Park, K. I. Piezoelectric Energy Harvesting from Two-Dimensional Boron Nitride Nanoflakes. *ACS Appl. Mater. Interfaces* **2019**, *11*, 37920−37926.
(34) Peng, Y.; Que, M.; Tao, J.; Wang, X.; Lu, J.; Hu, G.; Wan, B.; Xu, Q.; Pan, C. Progress in Piezotronic and Piezo-Phototronic Effect of 2D Materials. *2D Mater.* **2018**, *5*, No. 042003.
(35) Maity, K.; Mahanty, B.; Sinha, T. K.; Garain, S.; Biswasm, A.; Ghosh, S. K.; Manna, S.; Ray, S. K.; Mandal, D. Two-Dimensional Piezoelectric MoS_2-Modulated Nanogenerator and Nanosensor Made of Poly(vinlydine fluofide) Nanofiber Webs for Self-Powered Electronics. *Energy Technol.* **2017**, *5*, 234−243.
(36) Bertolazzi, S.; Brivio, J.; Kis, A. Stretching and Breaking of Ultrathin MoS_2. *ACS Nano* **2011**, *5*, 9703−9709.
(37) Zhan, Y.; Liu, Z.; Najmaei, S.; Ajayan, P. M.; Lou, J. Large-Area Vapor-Phase Growth and Characterization of MoS_2 Atomic Layers on a SiO_2 Substrate. *Small* **2012**, *8*, 966−971.
(38) Gao, Y.; Liu, Z.; Sun, D. M.; Huang, L.; Ma, L. P.; Yin, L. C.; Ma, T.; Zhang, Z.; Ma, X. L.; Peng, L. M.; Cheng, H. M.; Ren, W. Large-Area Synthesis of High-Quality and Uniform Monolayer WS_2 on Reusable Au Foils. *Nat. Commun.* **2015**, *6*, No. 8569.
(39) Zhang, W.; Chiu, M. H.; Chen, C. H.; Chen, W.; Li, L. J.; Wee, A. T. S. Role of Metal Contacts in High-Performance Phototransistors Based on WSe_2 Monolayers. *ACS Nano* **2014**, *8*, 8653−8661.
(40) Duerloo, K.-A. N.; Ong, M. T.; Reed, E. J. Intrinsic Piezoelectricity in Two-Dimensional Materials. *J. Phys. Chem. Lett.* **2012**, *3*, 2871−2876.
(41) Manzeli, S.; Allain, A.; Ghadimi, A.; Kis, A. Piezoresistivity and Strain-Induced Band Gap in Atomically Thin MoS_2. *Nano Lett.* **2015**, *15*, 5330−5335.
(42) Lu, X.; Utama, I. B.; Lin, J.; Gong, X.; Zhang, J.; Zhao, Y.; Pantelides, S. T.; Wang, J.; Dong, Z.; Liu, Z.; Zhou, W.; Xiong, Q. Large-Area Synthesis of Monolayer and Few-Layer $MoSe_2$ Films on SiO_2 Substrates. *Nano Lett.* **2014**, *14*, 2419−2425.
(43) Li, P.; Zhang, D.; Wu, J.; Cao, Y.; Wu, Z. Flexible Integrated Black Phosphorus Sensor Arrays for High Performance Ion Sensing. *Sens. Actuators, B* **2018**, *273*, 358−364.
(44) Wang, Z. L.; Song, J. Piezoelectric Nanogenerators Based on Zinc Oxide Nanowire Arrays. *Science* **2006**, *312*, 242−246.
(45) Ma, Z.; Li, S.; Wang, H.; Cheng, W.; Li, Y.; Pan, L.; Shi, Y. Advanced Electronic Skin Devices for Healthcare Applications. *J. Mater. Chem. B* **2019**, *7*, 173−197.
(46) Ghosh, S. K.; Adhikary, P.; Jana, S.; Biswas, A.; Sencadas, V.; Gupta, S. D.; Tudu, B.; Mandal, D. Electrospun Gelatin Nanofiber Based Self-Powered Bio-E-Skin for Health Care Monitoring. *Nano Energy* **2017**, *36*, 166−175.
(47) Liu, Y.; Zheng, H.; Zhao, L.; Liu, S.; Yao, K.; Li, D.; Yiu, C.; Gao, S.; Avila, R.; Pakpong, C.; Chang, L.; Wang, Z.; Huang, X.; Xie, Z.; Yang, Z.; Yu, X. Electronic Skin from High-Throughput Fabrication of Intrinsically Stretchable Lead Zirconate Titanate Elastomer. *Research* **2020**, *2020*, No. 1085417.
(48) Maity, K.; Garain, S.; Henkel, K.; Schmeiber, D.; Mandal, D. Self-Powered Human Health Monitoring Through Aligned PVDF Nanofibers Interfaces Skin-Interactive Piezoelectric Sensor. *ACS Appl. Polym. Mater.* **2020**, *2*, 862−878.

https://dx.doi.org/10.1021/acsami.0c18028
ACS Appl. Mater. Interfaces 2020, 12, 58132−58139